Voltage-Dependent Excitation Dynamics in UV-absorbing Organic Photovoltaics with Efficient Charge Transfer Exciton Emission

Quinn C. Burlingame,[1,*,†] Xiao Liu,[2,*] Melissa L. Ball,[1] Barry P. Rand,[1,2] and Yueh-Lin Loo[3,†]

* Q.C.B. and X.L. contributed equally to this work

[1] Andlinger Center for Energy and the Environment, Princeton University, Princeton, NJ, USA

[2] Department of Electrical and Computer Engineering, Princeton University, Princeton, NJ, USA

[3] Department of Chemical and Biological Engineering, Princeton, NJ, USA

[†] Correspondence: qb@princeton.edu, lloo@princeton.edu

Abstract

Intermolecular charge-transfer excitons play a central role in determining the performance of organic solar cells as their voltage-dependent formation, dissociation, and recombination dynamics contribute to photocurrent generation, radiative/nonradiative voltage losses, and photovoltaic fill factor. Here, we explore the properties of brightly-emitting wide energy gap (>2 eV) charge transfer excitons by measuring the voltage-dependent photoluminescence, photocurrent, and ultrafast pump-probe transient absorption spectra of organic solar cells employing five UV-absorbing donor molecules that differ only by the length of the oligophenylene or acene group at their core. We find that organic solar cells with a strong correlation between their voltage-dependent photocurrent and charge-transfer exciton photoluminescence have low photovoltaic fill factors as they require voltage to facilitate efficient charge-transfer exciton dissociation. In contrast, solar cells that are efficient can readily generate charges without an applied field and have a separate population of tightly-bound charge-transfer excitons that are responsible for emission. Considering that the sum of all excitation loss rates (*i.e.*, recombination and charge extraction) must be equal to the excitation generation rate in steady state, these voltage-dependent data allow us to solve for the voltage-dependent fate of all excitations in the solar cells and estimate upper and lower bounds for geminate and non-geminate recombination, respectively.

I. Introduction

For more than 25 years,[1] materials innovations and improved device architectures have consistently increased the performance of organic photovoltaics (OPVs), transforming them into a promising power source for (semi)transparent,[2–4] flexible,[5,6] and indoor applications[7,8] with

long-term potential as an environmentally-friendly electricity generation technology. With the recent emergence of high-performance non-fullerene acceptors, significant attention has turned to understanding and reducing energy losses *via* charge transfer excitons (CTEs) that form at photoactive donor-acceptor (D-A) heterojunctions (HJs).[9–17] Interfacial CTEs impact virtually every property of interest in OPVs as they mediate between monomolecular Frenkel excitons and free polarons and are frequent sites of both geminate and nongeminate recombination. Despite their importance, direct spectroscopic observation is challenging in most HJs as their luminescence is typically dim with quantum yields <0.01%, and their transitions can be obscured in optical absorption/emission spectra by overlapping monomolecular features. With emission yields >1%, organic HJs with wide energy gaps can break this paradigm as the so-called energy gap law[16,18–20] dictates that electron-phonon coupling – and thus the rate of nonradiative recombination – decrease as a function of energy gap.[16,21,22]

While wide energy gap organic HJs have been used for organic light-emitting diodes with low turn-on voltages,[21,22] recent interest in transparent solar cell applications has also stimulated OPV research with these materials.[4,16,23–26] One such HJ, between donor BF-DPB and acceptor B4PymPm, was recently demonstrated to efficiently generate charges in high-voltage OPVs (open-circuit voltage (V_{OC}) > 2V) with very low nonradiative energy losses (<0.4 eV) and high photovoltaic fill factors (*FF* = 70%).[16] To shift the absorption cutoff of these OPVs, we synthesized four triarylamine donor molecules that constitute two series, as shown in **Fig. 1a**—an acene series with a phenyl-core donor (BF-DP**P**), a naphthalene-core donor (BF-DP**N**), and an anthracene-core donor (BF-DP**A**), and an oligophenylene series that includes the same phenyl-core donor (BF-DP**P**), the commercially available bi-phenyl core donor (BF-DP**B**), and a terphenyl-core donor (BF-DP**T**).[4] Despite similarities in the structure of these donors, their photovoltaic performance when paired with acceptor B4PymPm is highly variable with devices exhibiting *FF*s that range from 40% to 74%.[4]

Heterojunctions comprising the five donor molecules employed in this work exhibit bright CTE emission, which we exploit to examine their excitation dynamics with optoelectronic and spectroscopic characterizations including transient absorption spectroscopy, *in operando* voltage-dependent transient absorption spectroscopy, and simultaneous voltage-dependent photoluminescence (PL) and photocurrent measurements. Quantifying voltage-dependent PL and photocurrent, we find that OPVs comprising donors with the largest cores (BF-DPT and BF-DPA) have strong correlations between these two quantities and exhibit low fill factors. The highest performing solar cell, which comprises donor BF-DPB, exhibits the weakest correlation

between its PL and photocurrent among the OPVs studied, suggesting that its CTE emission and photocurrent originate from separate populations (*i.e.*, tightly bound CTEs and polarons that dissociate without field assistance), which seems to be a requisite for efficient photovoltaic operation. In all solar cells, large reverse biases produce a strong correlation between PL quenching and photocurrent. We attribute this correlation to tightly bound CTEs that require voltage to dissociate and be extracted from the device. Imposing a simple conservation model whereby the sum of all excitation losses (*i.e.*, recombination and charge extraction) must be equal to excitation generation in steady state, we can solve for the voltage-dependent fate of all excitations in the solar cells and estimate upper and lower bounds for geminate and non-geminate recombination, respectively.

II. Results

Figure 1a shows the molecular structures of the five donor molecules and the acceptor molecule used in this work. The highest occupied molecular orbital (HOMO) and lowest unoccupied molecular orbital (LUMO) energies for each of these molecules were previously measured and are shown in **Fig. 1b**.[4] The optical energy gaps ($E_{G,opt.}$) were extracted from the absorption spectra in M.L. Ball *et al.*[4] and are given in **Table 1**. The PL spectra of blended HJs with each donor and acceptor B4PymPm are broad and featureless as shown in **Fig. S1a-e**—a signature of CTE emission,[27–29] except for that of BF-DPA:B4PymPm (**Fig. S1e**), which exhibits a high-energy shoulder around 2.5 eV. The energy of CTEs were extracted for each HJ by taking the intersection of the reduced EL and EQE spectra measured on OPVs with the structure shown in **Fig. S1f**.[30] The reduced spectra and their intersections are shown in **Fig. S1a-e** and the extracted CTE energies are given in **Table 1**. Since the BF-DPA:B4PymPm EQE spectrum in **Fig. S1e** does not have a visible CTE shoulder, we did not report a value for its CTE energy. We note that this method of determining the CTE energy is highly approximate,[31] as CTEs are very broad (>1.5 eV in the spectra shown in **Fig. S1a-e**) and the CTE populations are expected to be far from thermal equilibrium in the disordered HJs studied here.[32] Furthermore, the Gaussian fits to the low energy portion of the EQE spectra are poor, as can be seen in **Fig. S1a-d**,[33,34] suggesting that the tail of the CTE density of states (DoS) in all five HJs studied here is non-Gaussian. The driving force (ΔE) for charge transfer is defined as the difference between the energy of the donor singlet (S_1, approximated here by $E_{G,opt}$) and the CTE state of its HJ.[13,35,36] This value is approximated experimentally as the difference between the optical gap and CTE energy and is given in **Table 1**.

To gain computational insight into the energies and oscillator strengths of CTEs and to visualize the electron and hole densities that comprise them, density functional theory (DFT) was first employed to identify the lowest energy geometric configuration of each donor/acceptor pair, as described in **Methods**. Using this minimized energy geometry, the excited states for each donor/acceptor pair were calculated. The CTE energies and oscillator strengths from these calculations are given in **Table 1**. A visualization of the hole and electron densities composing a CTE between donor BF-DPB and acceptor B4PymPm in their lowest energy configuration is shown in **Fig. 1c**. For visual clarity, the two molecules and their associated orbitals have been spatially separated. The monomolecular triplet state (T_1) energies were also calculated for each donor and are provided in **Table 1**. A simplified Jablonski diagram showing the states considered in this work and their transition rates is shown in **Fig. 2**.

The PL quantum yield (PLQY) and PL transient response of each HJ was measured as described in **Methods**. The PLQY values are presented in **Table 1**, and the PL transients are plotted in **Fig. S2** with amplitude-averaged lifetimes extracted from bi-exponential fits shown in **Table 1**. The PL lifetime of BF-DPA:B4PymPm is significantly shorter than that of the others, which suggests that this HJ exhibits monomolecular singlet emission and/or strong CTE-singlet hybridization as well as additional nonradiative recombination.[37,38] Among the other four HJs, we observe correlations between the PLQYs, PL lifetimes, and DFT-calculated oscillator strengths in **Table 1**, with higher oscillator strengths correlated with higher PLQYs and lower PL lifetimes. However, given that most recombination is still nonradiative, variations in radiative recombination rate have a limited impact on the overall decay rate, and thus we can infer that the changes observed in **Fig. S2** are primarily driven by nonradiative rates. The PLQYs of these HJs (2.4% – 11.1%) are among the highest PL or electroluminescence (EL) quantum yields reported for CTE emission,[16,21,37–39] primarily due to the wide energy gaps of the constituent molecules and their CTEs.[16,18–20]

Solar cells comprising each of the five donors and acceptor B4PymPm were fabricated with the device architecture shown in **Fig. 3a** and characterized as described in **Methods**. The current density vs. voltage curves and external quantum efficiency (EQE) spectra of each OPV are shown in **Fig. S3**, with photovoltaic performance metrics summarized in **Table 2**. The voltage-dependent photocurrent and PL of each OPV was measured simultaneously using the setup shown in **Fig. S4,** and as described in **Methods**. All voltage-dependent PL spectra and representative normalized PL spectra at several operating voltages are shown in **Fig. S5**. The normalized spectra show that the CTE emission blue shifts with increasing reverse bias

across all five OPVs.[32] The PL intensity was calculated at each operating voltage by integrating the PL spectra across all wavelengths. **Figure 3b-f** shows the voltage-dependent PL intensity (red, left-axis) normalized to its value at open circuit, and the photocurrent (black, right-axis) normalized to its value at short circuit for the five OPVs. To directly compare the voltage-dependent photocurrent and PL intensity across materials systems, their normalized data are also plotted in **Fig. S6**. Since the intensity of the 408 nm laser diode is different than the broadband light source used for photovoltaic measurements, the open-circuit voltages here are slightly different than those listed in **Table 2,** and were determined by measuring the voltage at which photocurrent is zero: BF-DPP = 1.791 V, BF-DPB = 1.800 V, BF-DPT = 1.903 V, BF-DPN = 1.773 V, BF-DPA = 1.750 V. The responsivity of the OPVs was nearly constant with laser diode intensity, as shown in **Fig. S7** for a representative BF-DPA:B4PymPm device.

Ultrafast transient absorption measurements were performed on donor films and HJs with B4PymPm, as described in **Methods**. An example spectrogram showing the temporal evolution of the transient absorption spectrum of BF-DPB is shown in **Fig. 4a**, with the spectrograms for the other four donors shown in **Fig. S8a-e**. Each spectrogram was integrated over the wavelengths between the white horizontal lines in **Fig. S8a,c-e** to produce the integrated transient data in **Fig. S8f**. The observed lifetimes (on the order of 10-100 ps from **Fig. S8f**) are considerably shorter than those in **Table 1** extracted from PL transients, presumably because of exciton-exciton annihilation under the high excitation pump fluence. However, they are similar to those recently reported for nonfullerene acceptors, such as IT-4F, with a reported lifetime of 51 ps.[40] In some films, such as BF-DPB, BF-DPT, and BF-DPA, spectral shifts are observed shortly after excitation which suggests that species such as excimers may be forming in addition to monomolecular singlets.

Transient absorption spectrograms of BF-DPB:B4PymPm are shown shortly after excitation (<6 ns) in **Fig. 4b,** and at longer times (up to 500 ns) in **Fig. 4c**. Spectrograms of the other four HJs over the same durations are shown in **Fig. S9a,c,g,h** and **S10a,c-e**, respectively, alongside integrated transients corresponding to the wavelength ranges we attribute to Frenkel excitons, CTEs, and polarons. An example of these wavelength ranges for BF-DPB:B4PymPm is shown in **Fig. 4b** with the horizontal red lines bounding the wavelength range integrated to produce the transients we assign to Frenkel excitons, and the white and green lines bounding the wavelength ranges we attribute to CTEs and polarons, respectively. These wavelength ranges were chosen to maximally isolate the different spectral features from each other rather than to fully encompass a single feature. These wavelength ranges and the integrated

transients they produce (**Figs. S9d,e,f,i,j** and **S10f,g**) were only used for visualization and had no impact on the global fits (as described in **Methods**) or lifetimes extracted. In each blended HJ film, the signal corresponding to the donor singlet (as observed in the spectra on neat donors) decays very rapidly, which we attribute to charge transfer to CTEs consistent with previous reports.[40,41] The lifetime of this quenching process was extracted from global fits and is labeled as τ_{CT} in **Table 3**. As these singlet signals decay, a corresponding rise with the same lifetime is observed in the transient absorption spectra on blends, which we attribute to CTEs. We attribute the decay of this feature to dissociation of CTEs, with a globally-fitted lifetime of τ_{diss} in **Table 3**. In some spectra (BF-DPB, BF-DPT, and BF-DPA), a third feature is visible which grows in as the CTE signal decays (or bleaches in the case of the BF-DPA HJ). We attribute this feature to polaron absorption. As expected from previous descriptions,[33] the CTE and polaron populations fall into equilibrium with one another after several hundred picoseconds, eventually decaying with a single rate, τ_{decay} as shown in **Table 3**. The lifetimes attributed here to polaron/CTE decay (>3.9 ns) are far greater than those recently measured for nonfullerene acceptors (250 – 1700 ps),[40,41] presumably due to the large energy gaps of these HJs. Because the instantaneous power delivered during the 45 fs laser pulse is significantly larger than the 1000 W/m^2 in the AM1.5G solar spectrum, polaron-polaron and/or exciton-polaron annihilation may contribute to a shorter τ_{decay} than would be observed in the OPVs under real-world operating conditions. This explains why, despite polaron lifetimes of ~10 ns observed in transient absorption, the OPVs are able to efficiently extract charge when operating under typical solar intensities.

To observe how the excitation dynamics change as a function of applied voltage, full-stack transparent BF-DPB:B4PymPm OPVs were fabricated as described in **Methods** with the structure shown in **Fig. S11k**. Transient absorption spectra were collected over 6 ns to produce the spectrograms in **Fig. S11a-c,g,h**. Using the same wavelength integration ranges as those employed for the BF-DPB:B4PymPm thin film in **Fig. 4b**, transients corresponding to the Frenkel exciton, CTE, and polaron transient absorption signals are plotted in **Fig. 5** at five different applied voltages: -20 V, -10 V, -5 V, 0 V (J_{SC}), and 1.8 V (V_{OC}). We do not observe any changes in the dynamics of Frenkel excitons with applied voltage; they all decay rapidly within the first several picoseconds as shown in **Fig. 5a**. A rise is observed in **Fig. 5a** at longer times (>10 ps) because polarons begin to form and absorb light at ~660 nm, which falls within the wavelength range we integrated for Frenkel excitons. The CTE and polaron transients depend

on the applied voltage, with both the CTE population decaying faster and the polaron population increasing faster at larger reverse biases.

III. Analysis

In steady state, the generation of excitons is balanced by the sum of recombination and extraction mechanisms illustrated in the Jablonski diagram in **Fig. 2**. These include the extraction of charges as photocurrent, decay of singlets to the ground state, radiative recombination of singlet CTEs, trap-assisted recombination of charges, and the nonradiative recombination of triplets, triplet CTEs, and singlet CTEs. Expressing the rate of each of these as a fraction of the exciton generation rate, G, as shown in Eq. 1 is a useful way to visualize the fate of all excitations in an OPV:

$$1 = \frac{[^1CTE]k_{r,S-CT}}{G} + \frac{[^1CTE]k_{nr,S-CT}}{G} + \frac{[^3CTE]k_{nr,T-CT}}{G} + \frac{[T_1]k_{nr,T}}{G} + \frac{[CS]k_{SRH}}{G} + \frac{J_{photo}(V)/q}{G} \quad (1)$$

where $[^1CTE]$ and $[^3CTE]$ are the densities of singlet and triplet CTEs, respectively, $k_{r,S-CT}$ is the radiative recombination rate of singlet CTEs, $k_{nr,S-CT}$ and $k_{nr,T-CT}$ are the nonradiative recombination rates of singlet and triplet CTEs, $[T_1]$ is the density of monomolecular triplet excitons, $k_{nr,T}$ is the decay rate of triplets, $[CS]$ is the density of free charges, k_{SRH} is the rate of trap-assisted Shockley-Read-Hall recombination, and $J_{photo}(V)/q$ is the photocurrent extracted from the OPV at an applied voltage, V, divided by the charge of an electron, q. Because the rate of donor singlet decay is much slower than the rate of charge transfer ($1/\tau_{CT}$ in **Table 3**), we assume that all generated singlet excitons are converted into CTEs. In addition, we assume that all recombination of monomolecular triplets and triplet CTEs is nonradiative, and that the populations of CTEs, triplets, and free charges are implicitly voltage dependent. A more detailed derivation of Eq. 1, starting from the rate equations of each state, is shown in **Supplemental Note 1**.

To calculate photocurrent as a fraction of G for each OPV, we assume that all excitations will be dissociated and extracted as charge at an arbitrarily large reverse bias. Exponentially extrapolating the voltage-dependent photocurrent of each OPV as shown in **Fig. S12a**, the asymptote ($J_{photo,max}$) is therefore equal to G, and thus dividing $J_{photo}(V)$ by this $J_{photo,max}$ produces $J_{photo}(V)/qG$ at all applied voltages—equivalent to the final term in Eq. 1. Since only CTE emission is observed, the radiative term in Eq. 1 ($[^1CTE]k_{r,S-CT}/G$) is equivalent to PLQY by definition (photons emitted per photon absorbed). At V_{OC}, photogenerated charges accumulate to balance the applied field producing a pseudo zero-field condition. To calculate

the voltage-dependent PLQY as shown in **Fig. S12b**, we thus multiply the zero-field PLQY (**Table 1**) by the V_{OC}-normalized PL intensity shown in **Fig. 3** at all voltages. Since G is equal to the sum of extraction, emission, and nonradiative recombination rates, we plot the fraction of each of these components as a function of voltage in **Fig. S12c-g** with the blue shaded area representing the fraction of G extracted, green representing the fraction emitted through CTEs, and red representing the fraction which recombines non-radiatively through singlet CTEs, triplet CTEs, monomolecular triplets, or via trap-assisted recombination.

While triplet CTE formation, triplet formation, and trap-assisted recombination primarily occur nongeminately *via* polaron recombination, singlet CTEs can be created both geminately and nongeminately *via* charge transfer from photoexcited singlets and polaron recombination, respectively. To provide an upper bound for geminate recombination, we therefore assert that if all excitations were either extracted as photocurrent or recombined geminately through singlet CTEs, there would be a solution to the equation $A \times PLQY(V) + J_{photo}(V)/qG = 1$, where A is a constant, since the voltage-dependent PLQY is proportional to the singlet CTE population *via*:

$$PLQY(V) = \frac{[^1CTE]k_{r,S-CT}}{G}, \quad (2)$$

and thus the sum of all radiative and nonradiative recombination through singlet CTEs is also proportional to the PLQY with G, $k_{r,S-CT}$, and $k_{nr,S-CT}$ being constants:

$$PLQY(V) \propto \frac{[^1CTE](k_{r,S-CT}+k_{nr,S-CT})}{G}. \quad (3)$$

Since solutions to $A \times PLQY(V) + J_{photo}(V)/qG = 1$ do not exist, we estimated the upper bound for geminate recombination by solving for the largest value of A that allows the expression: $A \times PLQY(V) + J_{photo}(V)/qG < 1$ to remain true at all voltages. These upper bounds are shown for each OPV as the red lines on **Fig. S12c-g**. The difference between the red lines and the green shaded areas representing emission is therefore the maximum amount of nonradiative geminate recombination, and the difference between the red lines and the blue shaded area representing photocurrent is the minimum amount of nongeminate recombination through all sources (triplets, triplet CTEs, singlet CTEs, and trap-assisted). The voltage-dependent fractions corresponding to the maximum amount of nonradiative geminate recombination and minimum amount of nongeminate recombination are plotted in **Fig. S12h** and **S12i**, respectively. Since several of the curves in **Fig. S12i** are non-monotonic with voltage, perhaps more physical solutions to the upper bound of geminate recombination and lower bound of nongeminate recombination can be found by solving $A \times PLQY(V) + J_{photo}(V)/qG < 1$ with the additional

monotonicity constraint: if $V_1 \geq V_2$, then $A \times PLQY(V_1) - J_{photo}(V_1)/qG \geq A \times PLQY(V_2) - J_{photo}(V_2)/qG$, where V_1 and V_2 are applied voltages. A version of **Fig. S12** with this monotonicity constraint applied is shown in **Fig. S13**.

To quantify the correlation between the voltage-dependent decrease in PL and the increase in photocurrent, we calculated the Pearson correlation coefficient[42] for these data collected from each OPV as follows:

$$\rho_{J_{photo}-PL} = \frac{n\sum J_{photo}(V)PL(V) - \sum J_{photo}(V)\sum PL(V)}{\sqrt{n\sum J_{photo}(V)^2 - \left(\sum J_{photo}(V)\right)^2}\sqrt{n\sum PL(V)^2 - (\sum PL(V))^2}}, \quad (4)$$

where n is the number of voltage-dependent PL and photocurrent data points collected for each OPV, $J_{photo}(V)$ is the photocurrent, and $PL(V)$ is the wavelength-integrated PL intensity. If photocurrent and PL are perfectly negatively correlated such that an increase in photocurrent produces a proportional decrease in PL, then $\rho_{J_{photo}-PL}$ will be -1. If the data were totally uncorrelated, $\rho_{J_{photo}-PL}$ will be 0. The values of $\rho_{J_{photo}-PL}$ are calculated as -0.793, -0.402, -0.883, -0.595, and -0.926 for BF-DPP, BF-DPB, BF-DPT, BF-DPN, and BF-DPA, respectively, and are reproduced in **Table 2** for comparison with photovoltaic performance metrics. We note that this single-coefficient approach is limited in that it does not provide information about how the correlation changes with voltage. From **Fig. 3b-f**, it is evident that the voltage-dependent correlation between PL and photocurrent is weakest around V=0 and becomes considerably stronger in all OPVs at large reverse biases. Furthermore, we note that this approach only allows for estimation of bounds for geminate and nongeminate recombination, and cannot be used to determine where within this range the actual geminate/nongeminate recombination fractions lie.

IV. Discussion

Varying the molecular structure of the triarylamine donor molecules as shown in **Fig. 1** led to several systematic changes in the photophysical properties of neat films as well as those of their HJs with B4PymPm. As reported previously,[4] the energy gaps of the compounds decrease in each of the two series of donors—those with oligophenylene cores (BF-DPP, BF-DPB, and BF-DPT) and acene cores (BF-DPP, BF-DPN, BF-DPA)—with increasing core size. This redshift is more pronounced in the acene series as demonstrated in **Table 1**, though the UPS-measured HOMO energies of all donor molecules remain within experimental error of each other (**Fig. 1b**). Conversely, both the simulated and experimentally-determined CTE energies

increase with increasing donor core size (**Table 1**). Interestingly, the energy-splitting between the EL and PL spectra measured on the same full-stack OPVs in **Fig. S1** seems to inversely correlate with donor core size as BF-DPP:B4PymPm has the largest splitting and HJs with BF-DPA and BF-DPT have the smallest. Energy splitting between EL and PL spectra has been observed across other materials systems.[32,43] In thermally-evaporated HJs that are morphologically homogeneous, like those explored here, EL/PL splitting is attributed to the thermal relaxation of electrically-injected charges, which can preferentially populate the low-energy tail of the CTE DoS. This scenario contrasts optically-generated CTEs, which populate the DoS uniformly.[32] The reduced energy splitting between these spectra in HJs with BF-DPA and BF-DPT implies that the photogenerated (geminate and nongeminate) CTE populations are closer to thermal equilibrium.

The calculated triplet energies of the acenes are smaller (2.5 eV for BF-DPN and 1.9 eV for BF-DPA) than those in the oligophenylene series and they decrease as core size increases. This opens the possibility for efficient energy transfer from triplet CTEs into monomolecular triplets,[17] especially in the case of BF-DPA where the triplet energy is below the CTE energy. This may explain the high-energy emission shoulder (**Fig. S1e**) observed in BF-DPA:B4PymPm films, as would CTE-singlet coupling/hybridization[15,37] as the singlet-CTE energy splitting (ΔE) is projected to be lower than the 500 meV experimentally-determined singlet-CTE hybridization threshold.[15]

Simultaneous measurement of voltage-dependent photocurrent and PL using the setup described in **Fig. S4** allows for direct comparison of the two measurements. If, for example, the state that is responsible for emission is also responsible for photocurrent generation, a decrease in one measurement would lead to a proportional increase in the other, with a correlation coefficient (*i.e.* slope; as calculated in **Analysis**) of -1. Here, we observe that the voltage-dependent trends in these two measurements are not perfectly correlated, with the reverse-bias increase in photocurrent generation outpacing PL quenching. This indicates that not all recombination occurs through singlet CTE states as otherwise the voltage-dependent trends in photocurrent and PL would align. Interestingly, we observe in **Table 2** that the OPV with the highest *FF* (BF-DPB) has the least correlation between its PL and photocurrent, while OPVs with the lowest *FF*s (BF-DPT and BF-DPA) have the strongest correlations. This observation suggests that for efficient photovoltaic operation, the population of CTEs responsible for emission is separate from the states that lead to charge generation and photocurrent. Examining the voltage-dependent data for the BF-DPB OPV in **Fig. 3c** (the most efficient device

studied here) at the V_{OC} (V = 1.8 V) and J_{SC} (V = 0 V) operating points, the PL intensity is very weakly coupled to photocurrent—decreasing by less than 16% while the photocurrent increases from 0 to J_{SC}. At large reverse biases, the voltage-dependent slope of the PL intensity and photocurrent asymptotically approach each other. This stronger correlation is observed in the operation of all OPVs, which we take to imply two things: firstly, that even the strongly-bound relaxed CTEs that are responsible for PL can be dissociated with sufficient voltage, and secondly, that at large reverse biases virtually all recombination proceeds through singlet CTEs.

While the decoupling of voltage-dependent PL and photocurrent correlates with higher efficiency in the OPVs studied here and in a previous study,[43] this decoupling is unlikely for solar cells approaching their intrinsic efficiency limit, because the presence of persistent PL that cannot be readily quenched with reverse bias indicates that some CTEs are not being dissociated and are thus unable to contribute to photovoltage and photocurrent. Indeed, a recent study found that in triple cation perovskite solar cells, the highest performing devices have perfect overlap between their voltage-dependent PL quenching and photocurrent since photoexcitation in perovskites directly produces free charges.[44] Thus, we hypothesize that there are three regimes of voltage-dependent PL/photocurrent coupling for solar cells with varying efficiencies. In low *FF* OPVs, such as those comprising BF-DPT and BF-DPA, as well as polymer:fullerene OPVs,[43] many geminate CTEs are tightly bound and do not readily dissociate at or near zero field. Applying voltage assists in the dissociation of these states,[45–48] generating an electron/hole pair for each dissociated CTE and creating a strong correlation between PL quenching and photocurrent. For higher *FF* OPVs, such as those comprising BF-DPB in this work, a significant fraction of CTEs dissociate without an applied field (*e.g.*, near short circuit), which in turn creates a population of polarons that can be extracted as photocurrent when a voltage is present, and leaves behind a secondary population of emissive CTEs that do not readily dissociate with voltage. This phenomenon produces a weak correlation between voltage-dependent PL and photocurrent. At the high efficiency limit (analogous to nonexcitonic solar cells),[44] virtually all CTEs dissociate into free charges without an applied field. In this case, photocurrent and PL compete for the same nongeminate population of polarons, and thus the strong inverse correlation between the two is restored. As described in **Analysis**, the upper bound for geminate nonradiative recombination and lower bound for nongeminate recombination can be estimated from the voltage-dependent PL and photocurrent data as shown in **Figs. S12** and **S13**.

Examining the charge-transfer and CTE dissociation rates in **Table 3** that were extracted from transient absorption spectra, we make several observations as a function of donor molecule structure. In the oligophenylene series, the rate of Frenkel exciton quenching by charge transfer increases with donor core size (BF-DPT > BF-DPB > BF-DPP) while the opposite trend is observed in the acene series (BF-DPP > BF-DPN > BF-DPA). In all cases, the charge transfer rates are > 3 orders of magnitude higher than the decay observed in neat donor films, consistent with the total quenching of monomer emission observed in these HJs (except for BF-DPA:B4PymPm). In the oligophenylene series, the rate of CTE dissociation decreases by ~2x with the addition of each phenyl ring while remaining orders of magnitude lower than the CTE decay rates measured with transient PL (**Fig. S2 and Table 1**) and transient absorption (**Fig. S10** and τ_{decay} in **Table 3**). This suggests that an equilibrium between the CTE and polaron populations will be reached faster than the timescale of excitation decay, and that, all else being equal, the steady-state CTE population will be lowest in the BF-DPP-containing OPV and highest in the BF-DPT counterpart due to differences in their CTE dissociation rates. In addition to the differences in the DFT-calculated CTE oscillator strengths, these differences in CTE population may partially explain why PLQY increases among HJs with oligophenylene series donors as the core size increases.

The *in operando* transient absorption measurements on the transparent BF-DPB OPV shown in **Fig. 5** and **Fig. S11** allow us to track changes in the excitation dynamics as a function of applied voltage. Like previous studies that show little or no voltage-dependent quenching of Frenkel exciton emission,[28,43,49] the lifetime of Frenkel excitons in the OPVs studied here is constant with voltage (**Fig. 5a**). We attribute this observation to the rapid exothermic charge transfer from Frenkel excitons to CTEs. In cases where the energy barrier to dissociate Frenkel excitons is high (*e.g.,* in a neat organic thin film), the dynamics are much slower and large applied fields are needed to effectively quench emission in such cases.[50–52] Consistent with the conclusions drawn from the voltage-dependent PL measurements on the BF-DPB-containing OPV (**Fig. 3c**), we only observe a small difference in the transient CTE (**Fig. 5b**) and polaron populations (**Fig. 5c**) across the photovoltaic operation voltages (J_{SC} to V_{OC}). Farther into reverse bias, a decrease in the transient CTE population is observed with a concomitant increase in the polaron population. At longer times, the slopes of CTE and polaron decay are similar, supporting the hypothesis that these populations reach an equilibrium and decay together once the polaron population is large enough that recombination into CTEs balances the rate of CTE dissociation.

V. Conclusions

In conclusion, the relatively large CTE energies of the five organic HJs explored in this work limit their nonradiative losses, allowing the CTEs to efficiently radiate with PLQYs between 2.4% to 11.1%. We leverage this bright emission to probe the voltage-dependent PL and photocurrent across OPVs comprising the five HJs. Interestingly, we observe that the correlation between voltage-dependent PL and photocurrent is indicative of photovoltaic performance—namely fill factor, with stronger correlations found in OPVs with low fill factors. Efficient OPVs, in contrast, have decoupled CTE populations that are responsible for emission and photocurrent generation. Additionally, these voltage-dependent data allow us to calculate the fate of all excitations in the OPVs and to estimate upper bounds for nonradiative geminate recombination and lower bounds for nongeminate recombination. *In operando* voltage-dependent transient absorption measurements on full-stack transparent OPVs show that while the charge transfer process from monomolecular excitons to CTEs is voltage independent, the CTE and polaron populations are inversely related with a clear voltage dependence. This work highlights the crucial role that voltage-dependent CTE dynamics play in determining the photovoltaic performance of OPVs.

Acknowledgements

The authors thank Saeed-Uz-Zaman Khan for valuable discussions and Jordan Dull for his assistance sublimation purifying the donor materials. The authors acknowledge the use of the Ultrafast Transient Absorption Facility in the Scholes group at Princeton. The authors acknowledge the use of Princeton University's Imaging and Analysis Center and clean room, which are partially supported by the Princeton Center for Complex Materials, a National Science Foundation (NSF)-MRSEC program (DMR-1420541). Q.C.B. is grateful to the Arnold and Mabel Beckman Foundation for supporting this work through an Arnold O. Beckman Postdoctoral Fellowship. X.L. and B.P.R. acknowledge support from BioLEC, an Energy Frontier Research Center funded by the U.S. Department of Energy, Office of Science, Basic Energy Sciences under Award #DE-SC0019370. B.P.R. acknowledges support from the U.S. Department of Energy, Office of Basic Energy Sciences under Award #DE-SC0012458. Y.-L.L. acknowledges support from the National Science Foundation, under grant #DMR-1627925. M.L.B. thanks Princeton's Presidential Postdoctoral Fellowship Program for funding.

Data Availability Statement

All data supporting this work is included in the manuscript and supplemental information and is available in tabular form from the corresponding authors upon reasonable request.

Author Contribution Statement

Q.C.B. and X.L. conceived of this work together. M.L.B. performed all chemical synthesis and purification, as well as density functional theory calculations. Q.C.B. fabricated all samples and devices and characterized the photovoltaic performance of OPVs. X.L. performed the 0-field spectroscopic characterization of all organic blends and devices including transient absorption measurements and global fitting. Q.C.B. and X.L. constructed the voltage-dependent PL/photocurrent measurement setup and collected the voltage-dependent data together. Q.C.B. wrote the manuscript with input from all co-authors. B.P.R. and Y.-L.L. supervised the project.

Competing Interests

The authors declare no competing interests.

References

1. C. W. Tang, *Appl. Phys. Lett.*, 1986, **48**, 183–185.
2. Y. Li, X. Guo, Z. Peng, B. Qu, H. Yan, H. Ade, M. Zhang and S. R. Forrest, *Proc. Natl. Acad. Sci.*, 2020, **117**, 21147–21154.
3. I. Burgués-Ceballos, L. Lucera, P. Tiwana, K. Ocytko, L. W. Tan, S. Kowalski, J. Snow, A. Pron, H. Bürckstümmer, N. Blouin and G. Morse, *Joule*, 2021, **5**, 2261–2272.
4. M. L. Ball, Q. Burlingame, H. L. Smith, T. Liu, S. R. Parkin, A. Kahn and Y.-L. Loo, *ACS Energy Lett.*, 2022, **7**, 180–188.
5. Y. Sun, M. Chang, L. Meng, X. Wan, H. Gao, Y. Zhang, K. Zhao, Z. Sun, C. Li, S. Liu, H. Wang, J. Liang and Y. Chen, *Nat. Electron.*, 2019, **2**, 513–520.
6. J. A. Hauch, P. Schilinsky, S. A. Choulis, R. Childers, M. Biele and C. J. Brabec, *Sol. Energy Mater. Sol. Cells*, 2008, **92**, 727–731.
7. H. K. H. Lee, Z. Li, J. R. Durrant and W. C. Tsoi, *Appl. Phys. Lett.*, 2016, **108**, 253301.
8. H. S. Ryu, S. Y. Park, T. H. Lee, J. Y. Kim and H. Y. Woo, *Nanoscale*, 2020, **12**, 5792–5804.
9. X. Liu, Y. Li, K. Ding and S. Forrest, *Phys. Rev. Appl.*, 2019, **11**, 024060.
10. M. Azzouzi, J. Yan, T. Kirchartz, K. Liu, J. Wang, H. Wu and J. Nelson, *Phys. Rev. X*, 2018, **8**, 31055.
11. C. Yang, J. Zhang, N. Liang, H. Yao, Z. Wei, C. He, X. Yuan and J. Hou, *J. Mater. Chem. A Mater*, 2019, **7**, 18889–18897.

12. C. Yan, S. Barlow, Z. Wang, H. Yan, A. K. Y. Jen, S. R. Marder and X. Zhan, *Nat. Rev. Mater.*, 2018, **3**, 18003.
13. J. Liu, S. Chen, D. Qian, B. Gautam, G. Yang, J. Zhao, J. Bergqvist, F. Zhang, W. Ma, H. Ade, O. Inganäs, K. Gundogdu, F. Gao and H. Yan, *Nat. Energy*, 2016, **1**, 16089.
14. J. Benduhn, K. Tvingstedt, F. Piersimoni, S. Ullbrich, Y. Fan, M. Tropiano, K. A. McGarry, O. Zeika, M. K. Riede, C. J. Douglas, S. Barlow, S. R. Marder, D. Neher, D. Spoltore and K. Vandewal, *Nat. Energy*, 2017, **2**, 17053.
15. X.-K. Chen, D. Qian, Y. Wang, T. Kirchartz, W. Tress, H. Yao, J. Yuan, M. Hülsbeck, M. Zhang, Y. Zou, Y. Sun, Y. Li, J. Hou, O. Inganäs, V. Coropceanu, J.-L. Bredas and F. Gao, *Nat. Energy*, 2021, **6**, 799–806.
16. S. Ullbrich, J. Benduhn, X. Jia, V. C. Nikolis, K. Tvingstedt, F. Piersimoni, S. Roland, Y. Liu, J. Wu, A. Fischer, D. Neher, S. Reineke, D. Spoltore and K. Vandewal, *Nat. Mater*, 2019, **18**, 459–464.
17. A. J. Gillett, A. Privitera, R. Dilmurat, A. Karki, D. Qian, A. Pershin, G. Londi, W. K. Myers, J. Lee, J. Yuan, S.-J. Ko, M. K. Riede, F. Gao, G. C. Bazan, A. Rao, T.-Q. Nguyen, D. Beljonne and R. H. Friend, *Nature*, 2021, **597**, 666–671.
18. R. Englman and J. Jortner, *Mol. Phys.*, 1970, **18**, 145–164.
19. A. Nitzan, S. Mukamel and J. Jortner, *J. Chem. Phys.*, 1975, **63**, 200–207.
20. M. Bixon, J. Jortner, J. Cortes, H. Heitele and M. E. Michel-Beyerle, *J. Phys. Chem.*, 1994, **98**, 7289–7299.
21. T.-C. Lin, M. Sarma, Y.-T. Chen, S.-H. Liu, K.-T. Lin, P.-Y. Chiang, W.-T. Chuang, Y.-C. Liu, H.-F. Hsu, W.-Y. Hung, W.-C. Tang, K.-T. Wong and P.-T. Chou, *Nat. Commun.*, 2018, **9**, 3111.
22. D. Chen, G. Xie, X. Cai, M. Liu, Y. Cao and S.-J. Su, *Adv. Mater.*, 2016, **28**, 239–244.
23. T. Liu, Q. C. Burlingame, J. C. Sorli, M. L. Ball, G. Cheng, N. Yao and Y. Loo, *Adv. Energy Mater.*, 2021, **11**, 2100225.
24. X. Jia, E. C. Baird, J. Blochwitz-Nimoth, S. Reineke, K. Vandewal and D. Spoltore, *Nano Energy*, 2021, **89**, 106404.
25. N. C. Davy, M. Sezen-Edmonds, J. Gao, X. Lin, A. Liu, N. Yao, A. Kahn and Y.-L. Loo, *Nat. Energy*, 2017, **2**, 829–829.
26. J. C. Sorli, P. Friederich, B. Sanchez-Lengeling, N. C. Davy, G. O. Ngongang Ndjawa, H. L. Smith, X. Lin, S. A. Lopez, M. L. Ball, A. Kahn, A. Aspuru-Guzik and Y. L. Loo, *J. Mater. Chem. C*, 2021, **9**, 1310–1317.
27. X. Liu, B. P. Rand and S. R. Forrest, *Trends Chem.*, 2019, **1**, 815–829.
28. A. Gonzalez-Rabade, A. C. Morteani and R. H. Friend, *Adv. Mater.*, 2009, **21**, 3924–3927.
29. T. Linderl, T. Zechel, A. Hofmann, T. Sato, K. Shimizu, H. Ishii and W. Brütting, *Phys. Rev. Appl.*, 2020, **13**, 024061.

30. K. Vandewal, K. Tvingstedt, A. Gadisa, O. Inganäs and J. v. Manca, *Phys. Rev. B*, 2010, **81**, 125204.
31. A. Melianas, N. Felekidis, Y. Puttisong, S. C. J. Meskers, O. Inganäs, W. M. Chen and M. Kemerink, *Proc. Natl. Acad. Sci.*, 2019, **116**, 23416–23425.
32. A. N. Brigeman, M. A. Fusella, B. P. Rand and N. C. Giebink, *Phys. Rev. Appl.*, 2018, **10**, 034034.
33. T. M. Burke, S. Sweetnam, K. Vandewal and M. D. McGehee, *Adv. Energy Mater.*, 2015, **5**, 1500123.
34. S.-U.-Z. Khan and B. P. Rand, *Phys. Rev. Appl.*, 2021, **16**, 044026.
35. M. Azzouzi, N. P. Gallop, F. Eisner, J. Yan, X. Zheng, H. Cha, Q. He, Z. Fei, M. Heeney, A. A. Bakulin and J. Nelson, *Energy Environ. Sci.*, 2022, **15**, 1256–1270.
36. M. S. Vezie, M. Azzouzi, A. M. Telford, T. R. Hopper, A. B. Sieval, J. C. Hummelen, K. Fallon, H. Bronstein, T. Kirchartz, A. A. Bakulin, T. M. Clarke and J. Nelson, *ACS Energy Lett.*, 2019, **4**, 2096–2103.
37. Y. Dong, H. Cha, H. L. Bristow, J. Lee, A. Kumar, P. S. Tuladhar, I. McCulloch, A. A. Bakulin and J. R. Durrant, *J. Am. Chem. Soc.*, 2021, **143**, 7599–7603.
38. Y. Liu, Z. Zheng, V. Coropceanu, J.-L. Brédas and D. S. Ginger, *Mater. Horiz.*, 2022, **9**, 325–333.
39. D. Chen, G. Xie, X. Cai, M. Liu, Y. Cao and S. J. Su, *Adv. Mater.*, 2016, **28**, 239–244.
40. Y. Dong, H. Cha, H. L. Bristow, J. Lee, A. Kumar, P. S. Tuladhar, I. McCulloch, A. A. Bakulin and J. R. Durrant, *J. Am. Chem. Soc.*, 2021, **143**, 7599–7603.
41. K.-N. Zhang, M.-S. Niu, Z.-N. Jiang, Z.-H. Chen, T. Wang, M.-M. Wei, C.-C. Qin, L. Feng, W. Qin, S.-K. So and X.-T. Hao, *Solar RRL*, 2020, **4**, 1900552.
42. K. Pearson, *Philos. Trans. R. Soc.*, 1896, **187**, 253–318.
43. K. Tvingstedt, K. Vandewal, F. Zhang and O. Inganäs, *J. Phys. Chem. C*, 2010, **114**, 21824–21832.
44. M. Stolterfoht, V. M. le Corre, M. Feuerstein, P. Caprioglio, L. J. A. Koster and D. Neher, *ACS Energy Lett.*, 2019, **4**, 2887–2892.
45. L. Onsager, *Phys. Rev.*, 1938, **54**, 554–557.
46. J. Frenkel, *Phys. Rev.*, 1938, **54**, 647–648.
47. C. L. Braun, *J. Chem. Phys.*, 1984, **80**, 4157–4161.
48. O. Rubel, S. D. Baranovskii, W. Stolz and F. Gebhard, *Phys. Rev. Lett.*, 2008, **100**, 196602.
49. S. Inal, M. Schubert, A. Sellinger and D. Neher, *J. Phys. Chem. Lett.*, 2010, **1**, 982–986.
50. V. I. Arkhipov, H. Bässler, M. Deussen, E. O. Göbel, R. Kersting, H. Kurz, U. Lemmer and R. F. Mahrt, *Phys. Rev. B*, 1995, **52**, 4932–4940.

51. J. Szmytkowski, W. Stampor, J. Kalinowski and Z. H. Kafafi, *Appl. Phys. Lett.*, 2002, **80**, 1465–1467.

52. V. I. Arkhipov and H. Bässler, *Phys. Status Solidi A*, 2004, **201**, 1152–1187.

Figures and Figure Captions:

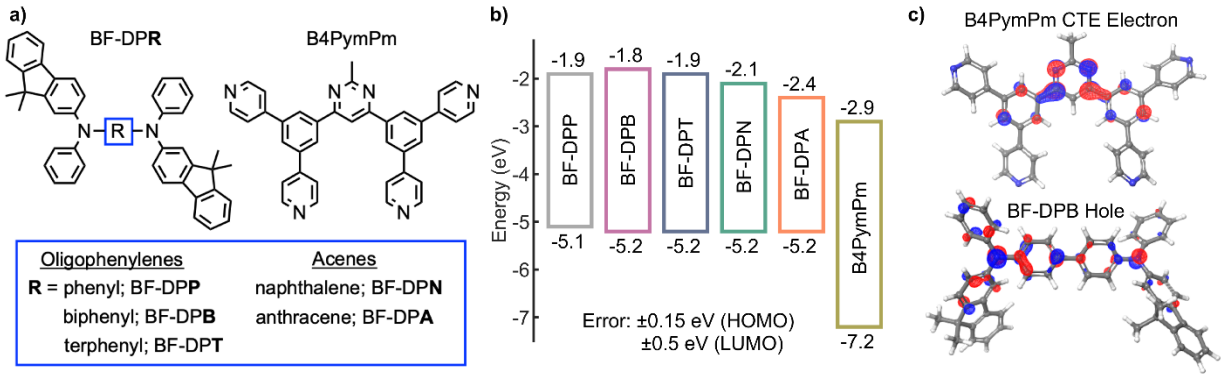

Figure 1 | Molecular structures, energy levels, and CTE visualizations. a) Molecular structures of acceptor B4PymPm and 5 donor molecules: BF-DPP, BF-DPB, BF-DPT, BF-DPN, and BF-DPA. **b)** Energy levels of the six materials in **a** measured by ultraviolet photoelectron spectroscopy and inverse photoemission spectroscopy.[4] **c)** Visualization of the DFT-simulated molecular orbitals that compose a CTE on a B4PymPm:BF-DPB pair in its lowest energy configuration. The molecules and orbitals are shown separately for clarity.

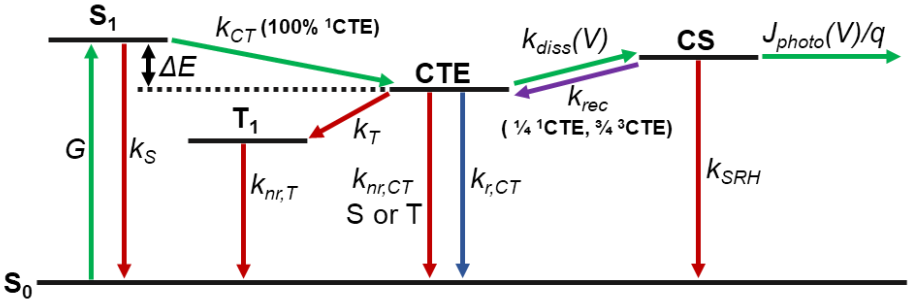

Figure 2 | Simplified Jablonski diagram showing state transitions. Simplified Jablonski diagram indicating the transitions between the ground state, S_0, Frenkel singlet excitons, S_1, CTEs which can be either singlet (^{1}CTE) or triplet (^{3}CTE), monomolecular triplet states, T_1, and charge separated (CS) states. The generation rate of singlets from optical absorption is denoted as G, the corresponding rate of singlet decay to S_0 is k_S, the rate of charge transfer from S_1 to the ^{1}CTE state is k_{CT}, the nonradiative and radiative recombination rates of CTE states are denoted respectively as $k_{nr,CT}$ and $k_{r,CT}$, the rate of transfer to T_1 from ^{3}CTE states is k_T, the voltage-dependent CTE dissociation rate is $k_{diss}(V)$, the recombination rate of separated charges back into CTE states is k_{rec}, and the rate of trap-assisted Shockley-Read-Hall recombination for charges is k_{SRH}. Monomolecular triplets are assumed to recombine exclusively non-radiatively with a rate $k_{nr,T}$. Voltage-dependent photocurrent extracted from the device constitutes a rate: $J_{photo}(V)/q$, where q is the charge of an electron.

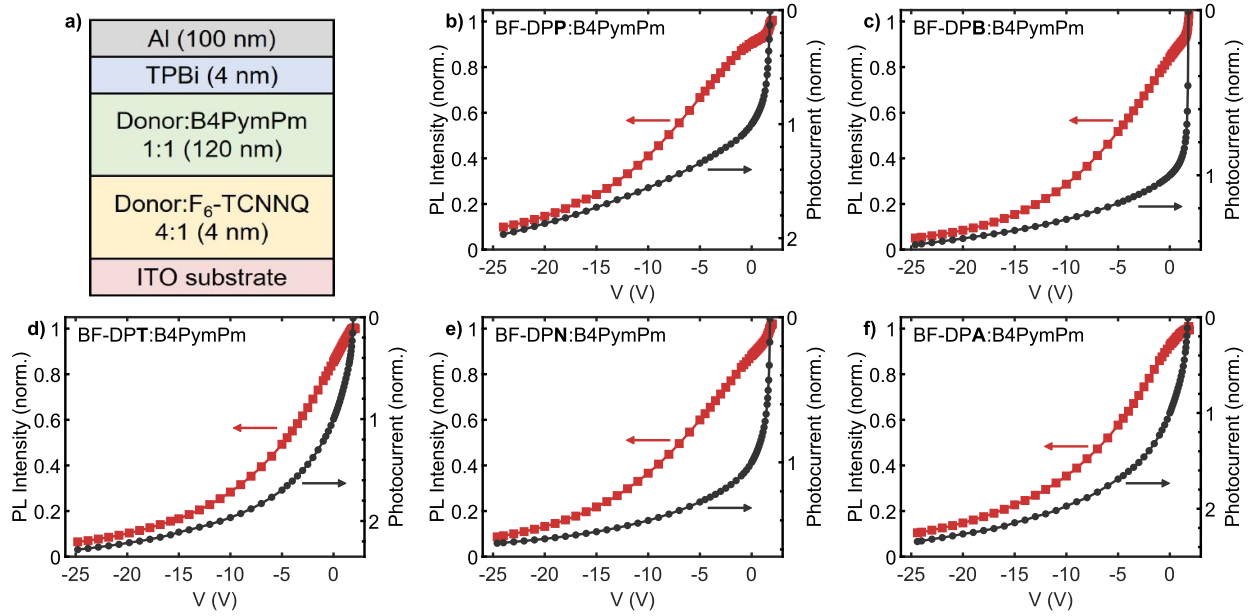

Figure 3 | Device structure and voltage-dependent photocurrent and PL. a) Device structure of non-transparent OPVs. **b-f)** Voltage-dependent photocurrent (black curves, right axes) and integrated PL intensity (red curves, left axes) measured on OPVs with the structure shown in **a** using the measurement setup shown in **Fig. S4**. Photocurrents were normalized to their value at V=0 (J_{SC}) for each device, while the integrated PL intensities were normalized to the intensity at open-circuit (V_{OC}). The full voltage-dependent PL spectra are shown in **Fig. S5**. To eliminate electroluminescence in the PL spectra under forward bias, the EL spectra were measured separately without the pump beam at voltages approaching and greater than V_{OC} where EL begins to be visible. The reference EL spectra were subtracted from the PL spectra at each voltage prior to integrating their intensity to generate the data shown here.

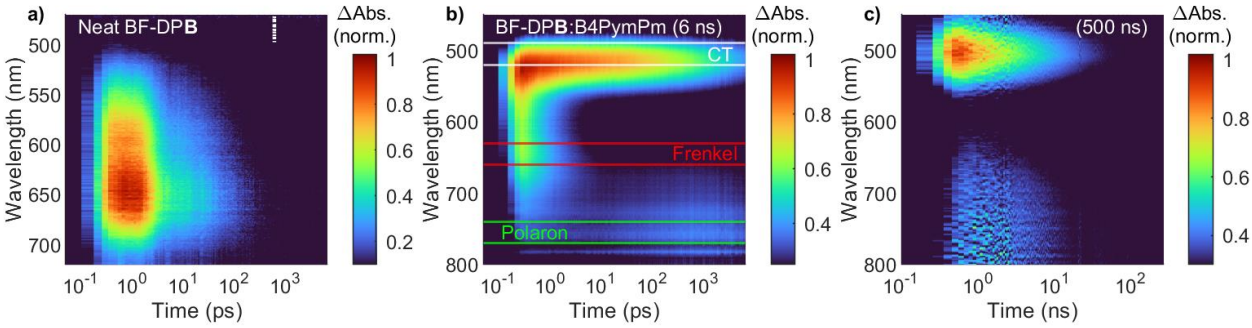

Figure 4 | Pump-probe transient absorption spectra and analysis. a) Transient absorption spectrogram measured on an 80-nm thick BF-DPB film. **b,c)** Transient absorption spectrograms of a 120-nm thick BF-DPB:B4PymPm HJ film measured for 6 ns after excitation and 500 ns after excitation, respectively.

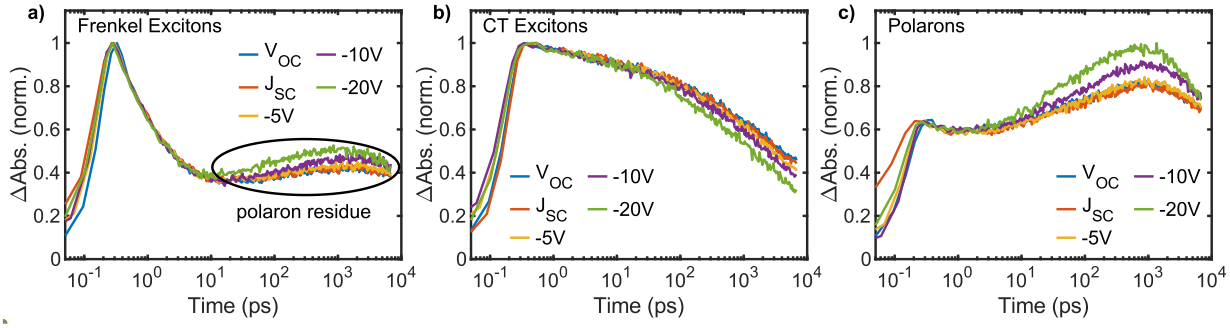

Figure 5 | Voltage-dependent transient absorption on transparent OPVs. Integrated transient spectra corresponding to the **a)** Frenkel exciton, **b)** CTE, and **c)** polaron absorption bands of a full-stack BF-DPB:B4PymPm transparent OPV with the structure shown in **Fig. S11k** at five different applied voltages: -20 V, -10 V, -5 V, 0 V (J_{SC}), and 1.8 V (V_{OC}). The full transient absorption spectra are shown in **Fig. S11**.

Tables and Table Captions:

Table 1 | State energies and analysis from absorption spectra, EL/EQE fitting, bulk HJ characterization, and DFT calculations.

Donor in Blend	Donor $E_{G,opt.}$ (eV)	CTE Energy (eV)	ΔE (eV)	DFT CTE Energy (eV)	DFT T_1 Energy (eV)	$PLQY$ (%)	$\tau_{PL,avg}$ (ns)	DFT oscillator strength
BF-DP**P**	3.05 ± 0.05	2.43	0.62	2.11	2.9	2.4	126	0.0012
BF-DP**B**	3.00 ± 0.05	2.54	0.46	2.19	2.9	4.7	90	0.0021
BF-DP**T**	2.97 ± 0.05	2.61	0.36	2.42	2.9	11.1	66	0.0073
BF-DP**N**	2.83 ± 0.05	2.46	0.37	2.15	2.5	2.9	86	0.0012
BF-DP**A**	2.45 ± 0.05	-	-	2.16	1.9	4.2	19	0.0021

Table 2 | Photovoltaic performance metrics of OPVs and Pearson correlation coefficients between voltage-dependent photocurrent and PL.

Active layer	J_{SC} (mA/cm^2)	V_{OC} (V)	FF (%)	PCE (%)	$\rho_{J_{photo}-PL}$
BF-DP**P**:B4PymPm	0.34	1.77	44.7	0.27	-0.793
BF-DP**B**:B4PymPm	0.82	1.80	58.7	0.87	-0.402
BF-DP**T**:B4PymPm	0.58	1.90	33.8	0.37	-0.883
BF-DP**N**:B4PymPm	0.73	1.77	45.2	0.58	-0.595
BF-DP**A**:B4PymPm	0.88	1.74	35.5	0.55	-0.926

*Performance variations were <3% for devices with the same geometry.

Table 3 | Rates from transient absorption fitting.

Donor	τ_{CT} (ps)	τ_{diss} (ps)	τ_{decay} (ns)
BF-DP**P**	1.5	111	16.5
BF-DP**B**	1.3	200	14.3
BF-DP**T**	0.8	356	50.8
BF-DP**N**	2.1	184	13.9
BF-DP**A**	6.6	166	15.2